

Review

Zelin Ma and Siddharth Ramachandran*

Propagation stability in optical fibers: role of path memory and angular momentum

<https://doi.org/10.1515/nanoph-2020-0404>Received July 19, 2020; accepted September 30, 2020;
published online October 21, 2020

Abstract: With growing interest in the spatial dimension of light, multimode fibers, which support eigenmodes with unique spatial and polarization attributes, have experienced resurgent attention. Exploiting this spatial diversity often requires robust modes during propagation, which, in realistic fibers, experience perturbations such as bends and path redirections. By isolating the effects of different perturbations an optical fiber experiences, we study the fundamental characteristics that distinguish the propagation stability of different spatial modes. Fiber perturbations can be cast in terms of the angular momentum they impart on light. Hence, the angular momentum content of eigenmodes (including their polarization states) plays a crucial role in how different modes are affected by fiber perturbations. We show that, accounting for common fiber-deployment conditions, including the more subtle effect of light's path memory arising from geometric Pancharatnam–Berry phases, circularly polarized orbital angular momentum modes are the most stable eigenbasis for light propagation in suitably designed fibers. Aided by this stability, we show a controllable, wavelength-agnostic means of tailoring light's phase due to its geometric phase arising from path memory effects. We expect that these findings will help inform the optimal modal basis to use in the variety of applications that envisage using higher-order modes of optical fibers.

Keywords: higher-order modes; multimode fibers; orbital angular momentum; Pancharatnam–Berry phase; vector beams; propagation stability.

1 Introduction

Multimode fibers (MMFs) and their spatially diverse higher-order modes (HOMs) have experienced alternating levels of interest ever since the invention of optical fibers. Although one of the first applications of light propagation, for image transport with flexible optical fiber waveguides, utilized MMFs [1], the development of single-mode fibers (SMFs) quickly diverted attention away from MMFs. One important reason was that any realistic deployment of optical fibers includes perturbations, such as bends, twists, 3D paths as well as thermal, mechanical, and environmental fluctuations. While modes in a perfectly straight, circular fiber are theoretically orthogonal, perturbations typically cause coupling between them, leading to potential loss of signal purity or information content. Subsequent advances in light guidance, including micro-structuring [2], photonic bandgaps [3], or antiresonant structures [4], primarily focused on means to strip out [5–7] HOMs to effectively realize single-mode guidance. In fact, even an SMF is two-moded, accounting for the two orthogonal polarization eigenmodes. As such, bend- or geometry-induced fiber birefringence [8] can cause polarization-mode dispersion in classical communications links [9] and loss of entanglement preservation in quantum links [10].

The advent of improved signal conditioning and reception technologies over the last decade has, however, refocused investigations on MMFs in which modes mix. Because this mixing predominantly represents unitary transformations, multi-in multi-out digital signal processing can disentangle mode mixing in the electronic domain [11], resulting in scaling the capacity of telecommunications links [12]. Analysis of the speckle patterns out of MMFs enables spectrometry [13]. On the other hand, adaptively controlling the speckle pattern at the input or output enables imaging with MMFs [14, 15]. Linear mixing, when combined with nonlinear coupling, leads to effects such as multimode solitons [16, 17], nondissipative beam cleanup [18] and geometric parametric instabilities [19], among a host of multimode nonlinear effects not seen in SMFs.

*Corresponding author: Siddharth Ramachandran, Boston University, Boston, MA, USA, E-mail: sidr@bu.edu. <https://orcid.org/0000-0001-9356-6377>

Zelin Ma, Boston University, Boston, MA, USA. <https://orcid.org/0000-0002-2801-4004>

The aforementioned benefits of a mixed ensemble of modes notwithstanding the ability to excite and propagate specific HOMs remain especially desirable. As is evident from any elementary solution of eigenmodes in waveguides, each HOM has a characteristic phase and group velocity, group-velocity dispersion, modal area (A_{eff}) [20, 21]. For instance, HOMs can be tailored to have large normal [22] or anomalous dispersion [23], with applications in dispersion control for telecom links [24, 25] and ultra-short pulses [26]. One of the first demonstrations of nonlinear wave mixing in optical fibers involved inter-modal phase matching between HOMs [27], the diversity of HOMs yielding enhanced degrees of freedom to achieve momentum conservation [28, 29]. Raman [30] or Briliouin [31] scattering have shown to be strongly dependent on, and hence be tailorably by, the mode(s) in which light propagates. These concepts have received increased attention for applications such as third-harmonic generation [32], extending supercontinuum generation [33], power-scalable source engineering [30, 34] or new forms of quantum sources [35]. The inherently large A_{eff} of HOMs has led to ultralarge A_{eff} , low-nonlinearity flexible fibers [36], with applications in fiber lasers [37]. More recently, fiber modes with orbital angular momentum (OAM) have been shown to yield an additional degree of freedom with which to control the nonlinear interactions of light in fibers [38–40]. Fiber sources operating in HOMs are also interesting for applications where a non-Gaussian-shaped emission is desired, such as in nanoscale microscopy [41, 42] and laser machining [43]. Finally, perhaps most significantly over the last few years, there has been an emerging realization that individual modes, especially those carrying OAM, can enable signal propagation with low or limited mode mixing [44], as a means of increasing the capacity of classical communications networks [45–48] or for enhancing the security of quantum links [49]. All these applications have two critical requirements: (1) the ability to accurately control mode transformations with, for instance, fiber gratings [50], diffractive optics [51], Pancharatnam–Berry optical elements (PBOE) [52], spatial light modulators [53], or metasurfaces [54]; and (2) crucially, the need for linearly, stably propagating desired modes in fibers.

Here, we address the latter issue – the propagation stability of optical fiber modes. Any realistic analysis of an optical fiber must necessarily consider the perturbations it encounters over the long lengths of signal transmission in facilitates. The key question is, in the presence of perturbations, how do otherwise theoretically orthogonal modes

of a cylindrically symmetric fiber mix with each other? This is a very complex problem for long-haul networks where propagation over 100s–1000s of kilometers of fiber encounters a wide array of stochastically varying perturbations. As a result, many realistic models for such mode coupling are phenomenological in nature [55, 56]. For shorter lengths, spanning a few meters to kilometers (lengths representing scales of fiber usage in most applications, such as fiber lasers and amplifiers, data-center links, nonlinear devices or sensors), this is a more tractable problem that can yield some first-principles insight. We show that certain classes of spatial modes are more stable and propagation-tolerant than others. Somewhat counter-intuitively, we also show that this stability depends even on the bases of modes used – that is, one set of modes can be more stable than modes represented in a mathematically equivalent but rotated basis. Fundamentally, we show that, accounting for typical perturbations an optical fiber encounters, the circularly polarized OAM eigenbasis represents the most stable set of modes for light transmission.

2 Mode classifications and fiber perturbations

2.1 Mode classifications

We start with a brief description of the eigenmodes of a cylindrically symmetric, step-index profile fiber. The 2D cross-section allows modes to be classified by two orthogonal polarization distributions, as well as a radial order index m , and an azimuthal order index L . Equation (1) shows the field distributions for the class of $L = 0$ modes ($\text{HE}_{1,m}$) in two polarization bases:

$$\mathbf{E}_{0,m} = e^{i\beta_{0,m}z} \cdot \left\{ \begin{bmatrix} \text{HE}_{1,m}^x \\ \text{HE}_{1,m}^y \end{bmatrix} \text{ or } \begin{bmatrix} \text{HE}_{1,m}^+ \\ \text{HE}_{1,m}^- \end{bmatrix} \right\} \quad (1)$$

where

$$\begin{bmatrix} \text{HE}_{1,m}^x \\ \text{HE}_{1,m}^y \end{bmatrix} = F_{0,m}(r) \begin{bmatrix} \hat{x} \\ \hat{y} \end{bmatrix}, \quad \begin{bmatrix} \text{HE}_{1,m}^+ \\ \text{HE}_{1,m}^- \end{bmatrix} = F_{0,m}(r) \begin{bmatrix} \hat{\sigma}^+ \\ \hat{\sigma}^- \end{bmatrix}$$

where $\hat{\sigma}^\pm = \hat{x} \pm i\hat{y}$, representing left or right handed circular polarization, respectively; $F_{0,m}(r)$ represents the radial profile of the field, which is typically a piecewise linear combination of Bessel functions for most profiles; β is the projection of the wave vector \vec{k} in the propagation direction (usually referenced by the mode's effective index,

$n_{\text{eff}} = \lambda\beta/2\pi$, where λ is the free-space wavelength of light). Paying attention to its subscripts, we see that β is distinct for each radial order m , but is identical for either polarization eigenmodes, represented in either bases. Modes designated as $\text{HE}_{L+1,m}$ (or $\text{EH}_{L-1,m}$, relevant for HOMs, described later) signify that fields of fiber modes are not strictly transverse to their propagation direction, but are, instead, a hybrid of electric and magnetic fields. This hybridization is typically negligible in weakly guiding fibers, where a scalar approximation leads to the commonly encountered linearly polarized (LP) modes, possessing a uniform, linear spatial polarization distribution. Similarly, we can have circularly polarized (CP) modes, denoting spatially uniform circular polarization distributions. For $L = 0$ modes in most weakly guided fibers, the scalar modes ($\text{LP}_{0,m}$ and $\text{CP}_{0,m}$) are almost identical to the vector modes $\text{HE}_{1,m}$ (with higher index contrast, this approximation breaks down, but, to first order, the field distributions remain the same, with only a small modification to β):

$$\widetilde{\mathbf{E}}_{0,m} = e^{i\widetilde{\beta}_{0,m}z} \cdot \left\{ \begin{bmatrix} \text{LP}_{0,m}^x \\ \text{LP}_{0,m}^y \end{bmatrix} \text{ or } \begin{bmatrix} \text{CP}_{0,m}^+ \\ \text{CP}_{0,m}^- \end{bmatrix} \right\} \quad (2)$$

where

$$\begin{bmatrix} \text{LP}_{0,m}^x \\ \text{LP}_{0,m}^y \end{bmatrix} = F_{0,m}(r) \begin{bmatrix} \hat{x} \\ \hat{y} \end{bmatrix}, \quad \begin{bmatrix} \text{CP}_{0,m}^+ \\ \text{CP}_{0,m}^- \end{bmatrix} = F_{0,m}(r) \begin{bmatrix} \hat{\sigma}^+ \\ \hat{\sigma}^- \end{bmatrix}$$

where the accent \sim denotes that the quantities have been calculated under the scalar approximation.

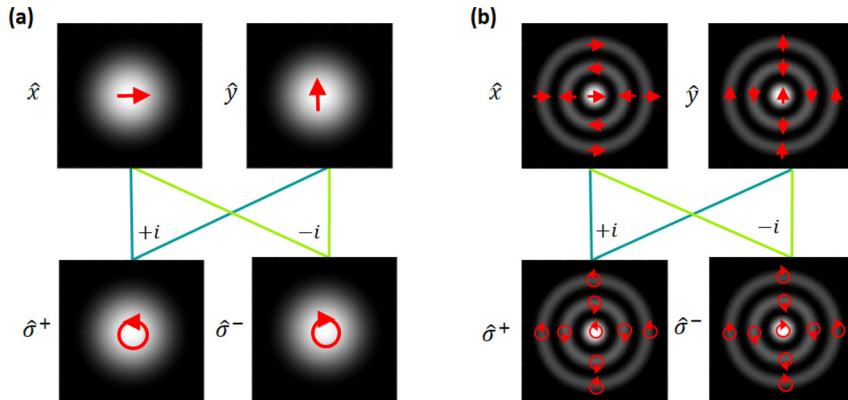


Figure 1: Field representations for $L = 0$ modes in a circular, step-index-guided fiber. Gray scale images show intensity distributions and red arrows indicate polarization state, either linear (straight arrows in top row) or circular (circular arrows in bottom row). The relationship between linear and circular polarizations are shown for the (a) $m = 1$ and (b) $m = 3$ modes. The colored lines indicate that the circular polarization modes can be represented as linear combinations of the two orthogonal linear polarization modes. The $+i$ or $-i$ terms represent a $\pi/2$ or $-\pi/2$ phase shift in the linear combinations. Conversely, linear polarization modes can be decomposed into two orthogonal circular polarization modes as well. The position where the arrowheads is shown within the circles representing circular polarizations are intentionally distinct, indicating a phase shift. Circular polarization representations where the arrowhead is on the top portion of respective circles is π phase-shifted from those in which they are on the bottom of the circle. This is a common feature of $\text{LP}_{0,m}$ or $\text{CP}_{0,m}$ modes – that each adjacent intensity ring of the mode accumulates a π phase shift and hence their fields are flipped.

Figure 1 shows the intensity profiles of two representative modes, with $L = 0$, and $m = 1$ and 3 , respectively, with $(m - 1)$ signifying the number of intensity nulls in the radial direction. Only the LP and CP modes are shown because the vector and scalar modes are almost identical for $L = 0$. The field with $L = 0$ and $m = 1$ is the well-known fundamental mode of SMFs. Linear combinations of the modes in any basis yield modes in another basis, as illustrated by the lines along with the $+i$ and $-i$ signs connecting modes of the different bases. Such linear combinations represent coordinate rotation among mutually unbiased bases (MUB), often used to transmit quantum information. Generally, the fundamental mode of SMFs and the entire class of $L = 0$ modes are twofold degenerate (in polarization) and any arbitrary polarization state of these modes propagates similarly in a fiber.

The situation is more complex for $L \neq 0$ modes. We leave aside the case of $|L| = 1$, which has its own peculiar behavior but which has been well-studied in the past [57]. Equation (3) shows the field distributions in two representations (assuming $L > 1$) similar to those used in Eq. (1):

$$\mathbf{E}_{L,m} = \left\{ \begin{bmatrix} \text{HE}_{L+1,m}^{\text{even}} e^{i\beta'_{L,m}z} \\ \text{HE}_{L+1,m}^{\text{odd}} e^{i\beta'_{L,m}z} \\ \text{EH}_{L-1,m}^{\text{even}} e^{i\beta''_{L,m}z} \\ \text{EH}_{L-1,m}^{\text{odd}} e^{i\beta''_{L,m}z} \end{bmatrix} \text{ or } \begin{bmatrix} \text{OAM}_{+L}^+ e^{i\beta'_{L,m}z} \\ \text{OAM}_{-L}^- e^{i\beta'_{L,m}z} \\ \text{OAM}_{+L}^- e^{i\beta''_{L,m}z} \\ \text{OAM}_{-L}^+ e^{i\beta''_{L,m}z} \end{bmatrix} \right\} \quad (3)$$

where

$$\begin{bmatrix} \text{HE}_{L+1,m}^{\text{even}} \\ \text{HF}_{L+1,m}^{\text{odd}} \\ \text{EH}_{L-1,m}^{\text{even}} \\ \text{EH}_{L-1,m}^{\text{odd}} \end{bmatrix} = F_{L,m}(r) \begin{bmatrix} \hat{x}\cos(L\varphi) - \hat{y}\sin(L\varphi) \\ \hat{x}\sin(L\varphi) + \hat{y}\cos(L\varphi) \\ \hat{x}\cos(L\varphi) + \hat{y}\sin(L\varphi) \\ \hat{x}\sin(L\varphi) - \hat{y}\cos(L\varphi) \end{bmatrix},$$

$$\begin{bmatrix} \text{OAM}_{+L}^+ \\ \text{OAM}_{-L}^- \\ \text{OAM}_{+L}^- \\ \text{OAM}_{-L}^+ \end{bmatrix} = F_{L,m}(r) \begin{bmatrix} \hat{\sigma}^+ \exp(iL\varphi) \\ \hat{\sigma}^- \exp(-iL\varphi) \\ \hat{\sigma}^- \exp(iL\varphi) \\ \hat{\sigma}^+ \exp(-iL\varphi) \end{bmatrix}$$

where $F_{L,m}(r)$ represents the radial profile of the fields, and φ is the azimuthal coordinate. In analogy with Eq. (1) (or Eq. (2)), the field is either linearly or circularly polarized at any specific transverse position in either representation. However, in contrast with the $L = 0$ modes, in one of the representations (HE/EH, also commonly called vector modes), the polarization distributions are spatially nonuniform. The uniformly circularly polarized mode basis is denoted as the OAM basis because the similarity of these fiber modes with free-space beams carrying OAM on

account of the helical phase $e^{iL\varphi}$ of the electric field [58]. These vector and OAM modes are illustrated in Figure 2, where the lines along with the $+i$ and $-i$ signs show the linear combinations that rotate modes from one basis to another. There are notable differences compared with the $L = 0$ modes. First, for each value of $|L|$ and m , there are four, instead of two, modes. Next, the propagation constants for the exact modes are not all degenerate, but instead depend on the internal symmetries of the modes. In the OAM basis, the modes are pairwise degenerate, but have different β s depending on whether signs of $\hat{\sigma}$ and L are the same (Spin-Orbit aligned – SOa – modes, with $\beta'_{L,m}$ shown in Eq. (3)) or if they are opposite (Spin-Orbit anti-aligned – SOaa – modes, with $\beta''_{L,m}$ shown in Eq. (3)). Correspondingly, in the vector basis, the β of the HE and EH modes differ. As in the case of the $L = 0$ modes shown in Figure 1, the SOa OAM modes and HE vector modes form an MUB and are linear combinations of one another, whereas the SOaa OAM modes and EH vector modes form a separate MUB.

Another, in fact, better known representation for the $L > 1$ modes is the LP designation, equivalent, as in the case of the $L = 0$ modes shown in Eq. (2), to the CP designation.

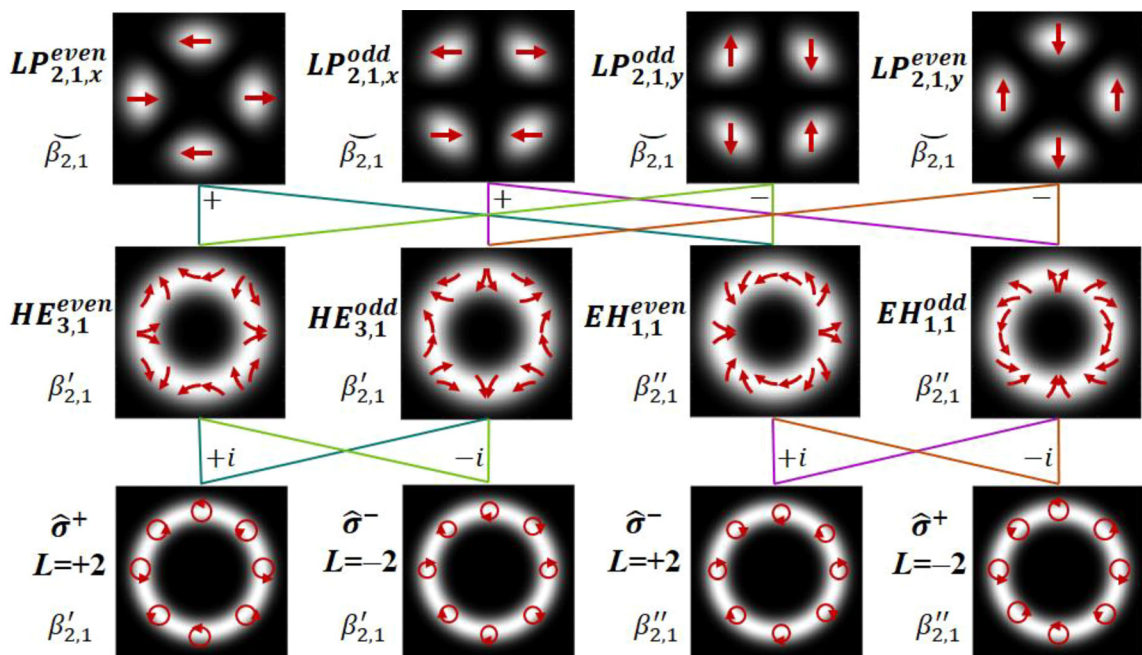


Figure 2: Intensity and polarization patterns of linearly polarized (LP) (top row), vector (middle row), and orbital angular momentum (OAM) modes (bottom row) with azimuthal index $|L| = 2$ and radial index $m = 1$. Colored lines show linear combinations between groups. The $+i$ or $-i$ terms represent a $\pi/2$ or $-\pi/2$ phase shift in the linear combinations. As described in the caption of Figure 1, azimuthal shifts of the arrows on the OAM modes indicate an azimuthal phase shift. The propagation constant is $\beta'_{2,1}$ for Spin-Orbit aligned (SOa) modes (and the corresponding HE modes), and $\beta''_{2,1}$ for SOaa modes (and the corresponding EH modes). The propagation constant of the LP designation is $\beta_{0,m}$, which is an average of $\beta'_{2,1}$ and $\beta''_{2,1}$.

Equation (4) shows the field distributions of this scalar designation in two representations similar to those used in Eq. (2):

$$\widetilde{\mathbf{E}}_{L,m} = e^{i\beta_{L,m} z} \cdot \left\{ \begin{bmatrix} \text{LP}_{L,m,x}^{\text{even}} \\ \text{LP}_{L,m,x}^{\text{odd}} \\ \text{LP}_{L,m,y}^{\text{odd}} \\ \text{LP}_{L,m,y}^{\text{even}} \end{bmatrix} \text{ or } \begin{bmatrix} \text{CP}_{L,m,+}^{\text{even}} \\ \text{CP}_{L,m,+}^{\text{odd}} \\ \text{CP}_{L,m,-}^{\text{odd}} \\ \text{CP}_{L,m,-}^{\text{even}} \end{bmatrix} \right\} \quad (4)$$

where

$$\begin{aligned} \begin{bmatrix} \text{LP}_{L,m,x}^{\text{even}} \\ \text{LP}_{L,m,x}^{\text{odd}} \\ \text{LP}_{L,m,y}^{\text{odd}} \\ \text{LP}_{L,m,y}^{\text{even}} \end{bmatrix} &= F_{L,m}(r) \begin{bmatrix} \hat{x} \cos(L\varphi) \\ \hat{x} \sin(L\varphi) \\ \hat{y} \sin(L\varphi) \\ \hat{y} \cos(L\varphi) \end{bmatrix}, \\ \begin{bmatrix} \text{CP}_{L,m,+}^{\text{even}} \\ \text{CP}_{L,m,+}^{\text{odd}} \\ \text{CP}_{L,m,-}^{\text{odd}} \\ \text{CP}_{L,m,-}^{\text{even}} \end{bmatrix} &= F_{L,m}(r) \begin{bmatrix} \hat{\sigma}^+ \cos(L\varphi) \\ \hat{\sigma}^+ \sin(L\varphi) \\ \hat{\sigma}^- \sin(L\varphi) \\ \hat{\sigma}^- \cos(L\varphi) \end{bmatrix} \end{aligned}$$

These intensity and polarization pattern of these LP designations (the CP designation is ignored here as their relationship with LP counterparts is the same as that in the $L = 0$ cases) are illustrated in the first row of Figure 2. Again, lines along with the + and - signs show how they can also be represented as a linear combination of vector (or OAM) modes. As evident from Figure 2, in contrast to the exact solutions (vector/OAM modes), the LP basis for $|L| > 1$ modes is actually a mixture of two OAM or vector modes of *different* β s. This has consequences for mode stability, as elaborated in Section 3.

2.2 Fiber perturbations

Figure 3 schematically shows the n_{eff} for select modes with indices L and m in select index-guided fiber designs. The coupling efficiency η , between these modes is given by [59]:

$$\eta \propto \int \int \int \overline{F_{L,m}(r)} \cdot \overline{P_{\text{pert}}(r, \varphi, z)} \cdot \overline{F_{L',m'}^*(r)} \cdot e^{i(\beta - \beta')z} \cdot e^{i(L - L')\varphi} \cdot dA \cdot dz \quad (5)$$

where the perturbation term P_{pert} is a matrix, accounting for the fact that the fields here are vector instead of scalar quantities. The most common perturbation $\overline{P_{\text{pert}}}$, in a fiber is a bend, which induces birefringence (i.e., it has an

off-diagonal matrix element that mixes the orthogonal components of $\overline{F_{L,m}}$ and $\overline{F_{L',m'}}$), and imparts OAM (i.e., it has a matrix element of the form $e^{i\Delta L\varphi}$ that spans all ΔL , although $|\Delta L| = 1$ is often the strongest component). Note that, although this integral was written with fields described in the OAM basis shown in Eq. (3), similar behavior may be expected of the integral written in other bases, because, after all, they are rotated MUBs of one another. Much physical intuition can be gained from inspecting the form of this integral.

Coupling is expected to be highest for degenerate modes, that is, when $\beta = \beta'$. Referring back to Eq. (2) and Figure 1, this clarifies why any bend causes polarization mixing between the two degenerate $L = 0$ modes, including SMF. Coupling between symmetric and antisymmetric modes, with $|\Delta L| = 1$, also appears to be easy with bends, and circumventing this has involved several instances of fiber designs or the use of modes where the effective-index separation ($\beta - \beta'$) between desired and relevant undesired modes is exacerbated. The amount these modes should be separated depends on specific experimental conditions and modes of interest, but as a general rule, $\overline{P_{\text{pert}}}$, for a bent, flexible fiber comprises a z -dependent matrix element $e^{i2\pi z/L_c}$, where L_c is a correlation length representing characteristic beat lengths for the perturbations. Typically, $L_c \sim 1$ mm to 1 cm, and hence it is easy to see that Δn_{eff} between modes of $\sim 10^{-4}$ to 10^{-3} typically reduces the integral in Eq. (5), hence minimizing coupling. Early dispersion compensation efforts [60, 61] involved "W" fiber designs that separated the n_{eff} of the desired $\text{LP}_{0,2}$ mode from the $\text{LP}_{2,1}$ and $\text{LP}_{1,2}$ modes (Δn_{eff} denoted as red arrows in Figure 3) by $\Delta n_{\text{eff}} > 10^{-3}$. Simple step index fibers have a naturally mode-separating feature, where Δn_{eff} between a desired $\text{LP}_{0,m}$ and the undesired $\text{LP}_{1,m}$ or $\text{LP}_{1,m-1}$ modes monotonically increases with radial order m [36] (green arrows in Figure 3). This feature has been used for scaling the A_{eff} of fiber modes [62], and stable modes with $A_{\text{eff}} \sim 6000 \mu\text{m}^2$ and yet $\Delta n_{\text{eff}} > 5 \times 10^{-4}$ have now been demonstrated [63] for fiber laser applications. Ring-core designs [64] perform two functions that enable stable OAM mode propagation [65, 66]. Their high index steps [57, 67, 68] help exacerbate the mode separations between SOa and SOaa modes (or, equivalently, HE and EH modes) to the order of $\Delta n_{\text{eff}} > 5 \times 10^{-5}$ (blue arrow in Figure 3), and the thin ring helps minimize the number of other radial order modes [69] that might be accidentally degenerate (and hence inadvertently mix) with the desired OAM modes. This design methodology has analogies with spin-orbit coupling for electrons in confined potentials [70], and has enabled device length (> 10 m) fiber propagation of 24

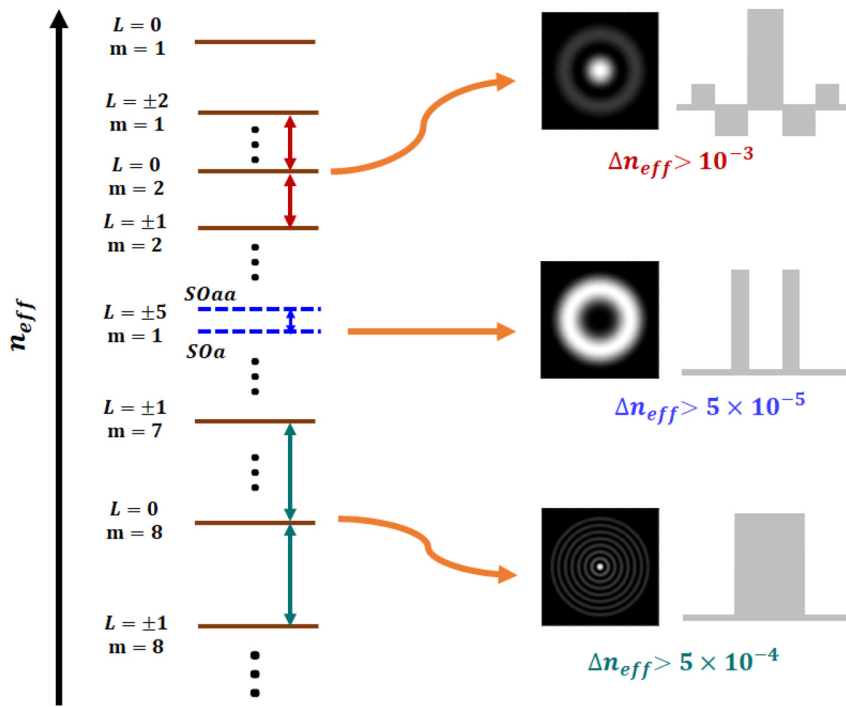


Figure 3: n_{eff} distributions for select modes with indices L and m . For visual clarity, not illustrated are polarization degeneracies of any of the modes or the n_{eff} degeneracies of any except for the $|L| = 5$ mode. Orange arrows leading to representative mode images for corresponding fiber designs (gray shaded features) describe mode separations (quantified by Δn_{eff}) for a select class of modes in their respective fibers. The n_{eff} of the $LP_{0,2}$ mode can be separated from $LP_{2,1}$ and $LP_{1,2}$ modes (red arrows) by using the class of “W” shape fiber designs, enabling its stable propagation for dispersion control designs. The n_{eff} splitting of $|L| = 5$ OAM modes (blue arrow) can be at least 5×10^{-5} in ring-core fiber designs, such that both $|L| = 5$ SOa and SOaa modes can propagate stably, yielding OAM mode stability in fibers. The n_{eff} splitting between $LP_{0,8}$ and its nearest neighboring $LP_{1,m}$ modes can be larger than 5×10^{-4} in simple step-index fibers (green arrows), enabling stable guidance of modes with large A_{eff} .

modes [69], to date. Equation (5) and the form of $\overline{\overline{P}_{\text{pert}}}$ point to an interesting mode stability criterion for OAM modes with high L indices. $\overline{\overline{P}_{\text{pert}}}$ from a bent fiber causes birefringence, and this is especially efficient in mixing two degenerate states of orthogonal polarizations – this was discussed in the context of $L = 0$ modes, which described why $LP_{0,m}$ modes seldom maintain polarization in a bent fiber. Because the cylindrical symmetry of an optical fiber implies that all modes have, at least, twofold (polarization) degeneracy (see Eqs. (1)–(4)), one expects this mixing to be commonly encountered, as in SMF or $LP_{0,m}$ modes. For low $|L|$ modes, this has indeed been observed [71]. But as $|L|$ of OAM modes increases, note that coupling between their degenerate counterparts additionally involves changing OAM from $+L$ to $-L$, that is, by $|\Delta L| = 2|L|$. Because $\overline{\overline{P}_{\text{pert}}}$ primarily induces $|\Delta L| = 1$ coupling, mixing between degenerate OAM modes reduces with $|L|$. Hence, even degenerate states of high $|L|$ OAM modes in suitably designed fibers do not mix [72]. That is, select modes can be polarization maintaining even in strictly circular fibers.

The (bend) perturbations considered thus far assumed in-plane redirection of light. Although it is possible to generalize Eq. (5) to consider more complex perturbations, considerable insight is obtained by independently considering the perturbation associated with a slow, adiabatic redirection of light in 3D space (out of plane). After all, this is a rather common perturbation encountered with a flexible fiber. Equation (5) suggests that, in the absence of other perturbations (bend-induced birefringence or angular momentum exchange, considered previously), such a slow, adiabatic change would have no effect. However, in fact, it does. The phase added by geometrical transformations is distinct from the more common propagating phase associated with βz of a beam of light. The discovery and exposition of this geometric phase, radically different from the propagating dynamic phase, dates back to the seminal report by S. Pancharatnam in 1956 [73]. It took ~ 30 years for its significance to be appreciated, awaiting the generalization of this concept in quantum mechanics by M. Berry [74]. One important manifestation of this concept is the spin-redirection phase demonstrated

by Tomita et al. [75]. A carefully constructed experiment with SMF showed that a fiber, configured to traverse a 3D route in space, acquired phase that was dependent only on the solid angle subtended by the fiber path in momentum (wavevector) space. The sign of this phase depends on the handedness of the circular polarization of a photon. Each degenerate mode in the $CP_{0,1}$ basis (see Eq. (2)) acquires a geometric phase ϕ_g of sign opposite to that of its polarization ($\hat{\sigma}^\pm$). This concept is intimately related to the idea that light carrying circular polarization denotes photons carrying spin angular momentum (SAM) [76], and that a 3D path of light imparts extrinsic angular momentum to it. Thus, an $LP_{0,1}$ mode, which is the linear combination of two orthogonal $CP_{0,1}$ modes, rotates under such geometric perturbations. Fundamentally distinct from the conventional dynamic phase (which includes, birefringence, angular momentum exchange, etc., discussed earlier) with dependence on propagation length, the geometric phase stores “memory” of the evolution (like geometry of the pathway) of a lightwave [77, 78]. The ray trajectory can be continuously deformed into any shape without changing the geometric phase as long as the solid angle remains unchanged, pointing to the topological nature of the effect. The composite effect of (bend-induced) birefringence as well as geometric perturbations on SMFs is illustrated in Figure 4. The first section of the fiber illustrates only a 3D path (geometric transformation – the fact that the fiber is lifted out of plane is schematically illustrated by a shadow it subtends, in-plane). This adds phase in the $CP_{0,1}$ basis, hence a single $CP_{0,1}$ mode merely acquires a phase. By contrast, the $LP_{0,1}$ mode rotates in polarization orientation. After that, the second section of the fiber illustrates a conventional bend that induces birefringence, which serves to convert both the $CP_{0,1}$ as well as $LP_{0,1}$ modes into modes with arbitrary elliptical polarization states.

The preceding analysis was restricted to the fundamental mode of SMF, that is, the $L = 0, m = 1$ mode (though similar behavior is expected for higher m $LP_{0,m}$ / $CP_{0,m}$ modes). In these modes, the only contribution to angular momentum arises from the polarization ($\hat{\sigma}^\pm$). This concept is extendable to beams carrying OAM in addition to SAM, and the resultant geometric phase is given by [79]:

$$\phi_g(C) = -(\sigma + L)\Omega(C) \quad (6)$$

where C represents the path contour, $\Omega(C)$ represents the solid angle subtended by this path in momentum space, and σ represents the handedness of circular polarization or amount of SAM, taking values of ± 1 for light with $\hat{\sigma}^\pm$, and all other quantities have been previously defined. As is evident, geometric phase is enhanced for OAM modes, and

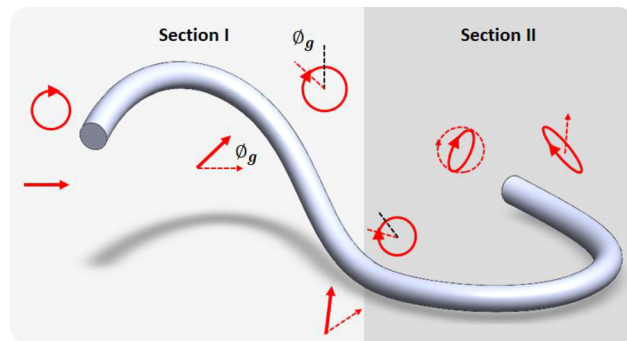


Figure 4: The effect of nonplanar and birefringent perturbations on the polarization of light launched into single-mode fibers (SMFs), illustrated as a flexed gray cylinder. Solid red arrows represent linear polarization states of light in the fiber at different positions along the propagation direction, with the dashed arrows denoting the state it possessed just before propagating to that position. Similarly, arrows on red circles represent circular polarization states and ellipses denote arbitrary elliptically polarized states. Mode transformations described below assume that light enters the fiber at the upper left end. The first section (I) represents an out-of-plane path (schematically illustrated by a shadow it subtends in plane) that is of large bending radii and hence free from fiber birefringence. The second section (II) represents an in-plane path that has strong birefringence. For a fundamental $CP_{0,1}$ mode with right-hand circular polarization, the nonplanar path imparts an extra phase ϕ_g due to geometric effects arising from Pancharatnam–Berry phases, but otherwise does not perturb the polarization state. This extra phase is illustrated by an azimuthal shift of the arrowhead. A mode with left circular polarization would behave similarly but accumulate an opposite phase ϕ_g . By contrast, a fundamental $LP_{0,1}$ mode with horizontal polarization, being a linear combination of the two orthogonal circular polarizations, is rotated by an angle ϕ_g along the nonplanar path. The subsequent bend of section II induces birefringence, and hence transforms any $LP_{0,1}$ or $CP_{0,1}$ mode into arbitrary elliptically polarized states, with ellipticity and handedness controlled by the strength of the bend-induced birefringence.

depends on the total angular momentum (TAM) of a photon. Observing this effect has historically been obscured by the fact that fiber modes experience all aforementioned dynamic and geometric perturbations simultaneously. One report [80], describing the strength of a so-called optical Magnus effect, showed that the speckle pattern out of a multimode fiber rotates when changing the sign of circular polarization, with the effect being proportional to the solid angle subtended by the fiber coil in the momentum space. A fiber in which low $|L|$ OAM or vector modes were excited showed [81] the rotation of polarizations pattern to be explicitly dependent on mode order L . Unfortunately, concurrent birefringent and angular momentum coupling implied that the experimentally observed rotation did not match the theory well because the SOa and SOaa modes also coupled due to bends and birefringence. In fact, the first experiment [75] with SMFs,

described earlier, emphasized the need for short fibers and large bending radii to observe the effect with reasonable fidelity.

3 Propagation stability experiments

The advent of ring-core fibers greatly aids the study of propagation effects in perturbed fibers because of the ability to isolate the effects of the disparate perturbations described in section 2. As described earlier, the ring-core fiber minimizes coupling within the mode group – that is, coupling between the SOa and SOaa pairs of modes (see Figure 3), and the angular momentum conservation effect forbids coupling between degenerate states for high enough $|L|$.

In this section, we describe experiments probing the propagation stability of different fiber modes. We do not consider the $L = 0$ LP or CP modes because the fundamental SMF mode has been well-studied and higher $LP_{0,m}$ / $CP_{0,m}$ modes essentially behave similarly in fibers where they are sufficiently isolated. We also limit ourselves to the study of $|L| > 1$ modes but with $m = 1$ because higher radial orders (higher m) modes also essentially behave similarly. We first consider modes in the LP basis, shown in the top row of Figure 2(a). Note that each LP mode is a linear combination of two vector or OAM modes of distinct propagation constants β' and β'' , respectively – indeed, this is the origin of the average $\bar{\beta}$ defined under this scalar approximation ($\bar{\beta} \sim \frac{\beta' + \beta''}{2}$). Hence, these modes are fundamentally unstable, in that their spatial patterns and polarizations rotate upon propagation, even in a strictly straight, perturbation-free fiber. This is evident from inspecting the two distinct LP mode images in Figure 2(a) arising from the addition or subtraction of nondegenerate vector or OAM modes – the nondegeneracy necessarily means that the phase difference between them oscillates with propagation. As such, LP modes of $L \neq 0$ are *never* stable in a fiber, and their use necessarily requires pre- or post-processing, optically or electronically, for information recovery.

Figure 5(a) shows the experimental setup [82] used for studying the mixing of two degenerate OAM or vector modes, in a 4-m long ring-core fiber [72] supporting stable propagation (i.e., without SOa–SOaa mixing) of high- $|L|$ modes ($|L| = 5, 6, 7$). The incoming Gaussian beam at 1550 nm from an external cavity laser (ECL) is converted into the desired OAM or vector mode using a PBOE called q -plate [52, 83]. A q -plate with topological charge q can

project circular polarization onto OAM modes of order $|L| = |2q|$, with the spin–orbit alignment dependent on the sign of q (Eq. (7)).

$$A\hat{\sigma}^+ + B\hat{\sigma}^- \xrightarrow{q} A\hat{\sigma}^- e^{i2q\varphi} + B\hat{\sigma}^+ e^{-i2q\varphi} \quad (7)$$

where the arrow denotes the transformation induced by the q -plate and A and B are mode amplitudes.

In the following representative experiments, we used $q = 7/2$, which causes Gaussian beams of two circular polarizations $\hat{\sigma}^+$ and $\hat{\sigma}^-$ to be converted into two degenerate SOaa OAM modes of $L = +7\hat{\sigma}^-$ and $L = -7\hat{\sigma}^+$, respectively. The purity of OAM modes excited in the fiber is confirmed to be greater than 15 dB via spatial interferometry [71]. The output of the ring-core fiber is then converted back to a fundamental Gaussian-shaped free-space modes using an identical q -plate. Thereafter, with appropriate polarization optics, the two orthogonal polarization components of the output beam can be spatially separated and projected onto a camera. Therefore, the power ratio between polarization bins on the camera represents the mixing ratio of two degenerate OAM modes in the fiber. By launching a pure mode into the fiber, its stability within the fiber can be deduced by measuring the relative power scattered into its degenerate counterpart. The combination of q -plate and wave plates can not only generate two degenerate OAM modes but also any of their linear combinations. Because linear polarizations are linear combinations of circular polarizations and vector modes are linear combinations of OAM modes, Gaussian beams with two orthogonal linear polarizations can be mapped onto two degenerate vector modes ($A = \pm B$ in Eq. (7)). Reciprocally, measuring the power ratio in the two linearly polarized bins yields the mode-mixing ratio between the two degenerate vector modes. By switching the polarization between circular and linear using quarter-wave plates (or their lack, thereof), we are able to switch between the OAM and vector modal bases with ease while maintaining all other experimental (perturbative) conditions. Representative experimental results on propagation stability in the presence of in-plane and out-of-plane bends are shown for the $|L| = 7$ SOaa OAM modes and the corresponding mathematically rotated basis of $EH_{6,1}$ odd and even modes.

The plots in Figure 5(c) and (d) show the measured power fluctuations between two degenerate OAM and vector modes, respectively, as the fiber is bent, in plane, as illustrated in Figure 5(b). When the input is an OAM mode ($L = -7\hat{\sigma}^+$), a negligible amount of power (~ 12 dB) is scattered to its degenerate counterpart. This is consistent with earlier observations that high $|L|$ OAM modes are stable, even between degenerate modes, in ring-core fibers [72]. For a vector mode input ($EH_{6,1}^{\text{even}}$), the power of parasitic degenerate mode ($EH_{6,1}^{\text{odd}}$) remains mostly low, at

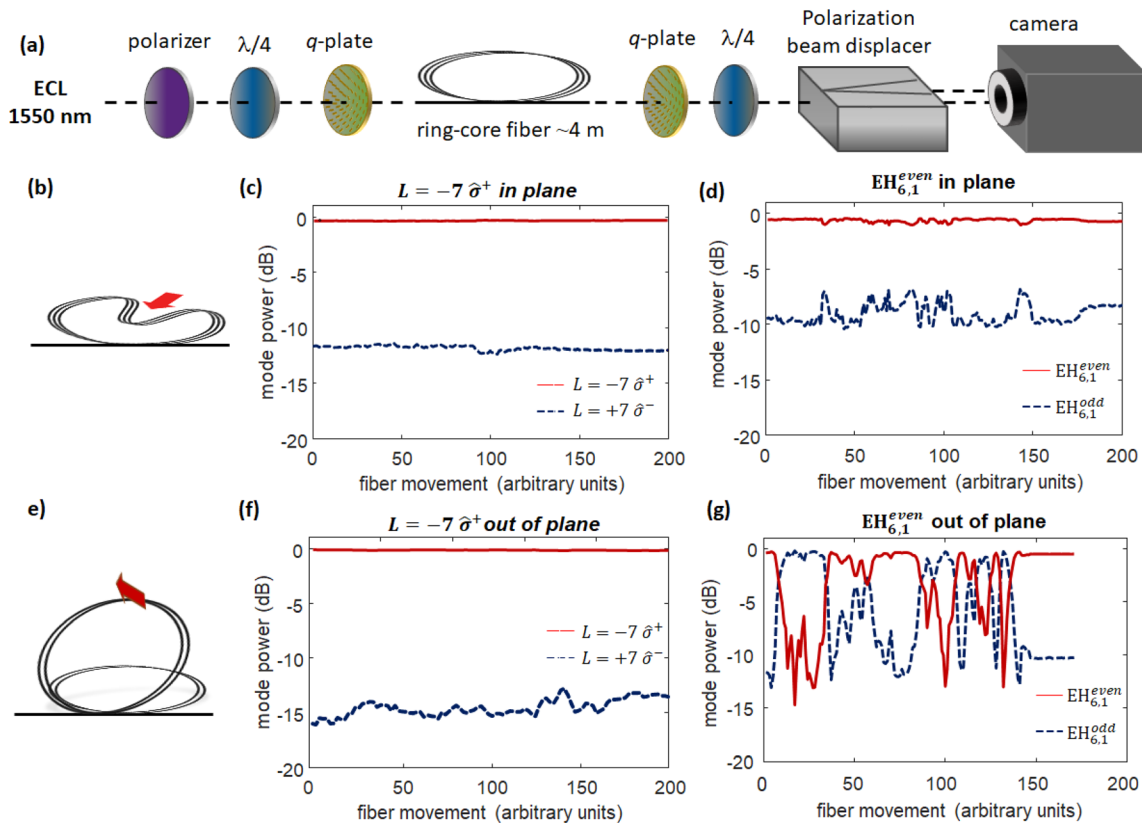


Figure 5: (a) Experimental setup used for studying the mixing ratio of two degenerate orbital angular momentum (OAM) or vector modes. For the OAM basis, the quarter-wave plate ($\lambda/4$) is rotated to an angle such that the fast axis is 45° with respect to the axis of polarizer to generate circularly polarized light, which is converted to OAM modes by the q -plate. In contrast, for the vector basis, the fast axis of the quarter-wave plate is aligned with the axis of the polarizer, such that linearly polarized light can be projected on to corresponding vector modes; A reciprocal setup at the fiber output converts the modes back to Gaussian beams, with the power in each polarization bin being proportional to the power of the individual degenerate (OAM or vector) modes at the fiber output. For the vector mode measurement, the output quarter-wave plate is removed. When measuring OAM mode stability, the input was a ~ 15 -dB pure $L = -7\hat{\sigma}^+$ mode, whereas, during the vector mode stability measurements, the input was a ~ 10 -dB pure $EH_{6,1}^{even}$ mode. (b) Schematic of fiber loops being bent in-plane to varying degrees, during the measurement. Part of the fiber loops (radius ~ 12 cm) are gradually bent into radius ~ 4 cm, and then return back to the original; (c) Plot of relative power in the two degenerate OAM modes ($L = \mp 7\hat{\sigma}^\pm$) under the application of perturbations as shown in (b); (d) Corresponding plot of relative power in the two degenerate $EH_{6,1}$ modes for in-plane perturbations; (e) Schematic of fiber partly (2 out of 4 fiber loops) being lifted out of plane to different heights during measurements. The plane of lifted fiber is moved to the plane perpendicular to the original and then moved back; (f) Plot of relative power in the two degenerate OAM modes ($L = \mp 7\hat{\sigma}^\pm$) as the fiber is moved out of plane, as shown in (e); (g) Corresponding plot of relative power in the two degenerate $EH_{6,1}$ modes for out-of-plane perturbations. OAM modes remain stable to bend as well as 3D perturbations, while the vector modes are completely mixed by 3D path redirections of the fiber.

the -10 dB level. Some power jumps to around -7 dB are evident. This is due the experimental inability of a strictly in-plane perturbation. Later, we will describe the origin of this discrepancy, but a higher level summary of these two experiments is that OAM and vector modes remain robust to degenerate mode coupling in the presence of in-plane bend perturbations. Given that OAM mode stability was already known [72], this was to be reasonably expected, given that its mathematically equivalent counterpart, the vector modes, would also possess similar stability. The plots in Figure 5(f) and (g) show the mode mixing between two degenerate OAM modes and vector modes as the fiber

is moved out of plane, as illustrated in Figure 5(e). Again, for the OAM mode input ($L = -7\hat{\sigma}^+$), the power of parasitic degenerate mode remains at a very low level (~ 14 dB). By contrast, when the input is the EH_{61}^{even} mode, the two degenerate modes completely mix with each other with 3D fiber perturbations.

This curious result, of two mathematically identical sets of modes behaving differently under 3D perturbations is a manifestation of the geometric phase discussed in section 2. An OAM mode traversing a nonplanar path (modified mode represented as \widetilde{OAM}) obtains an extra phase factor compared with the input (Eq. (8)). As two

degenerate OAM modes have opposite sign of L and σ , the geometric phases they accumulate, as per Eq. (6), have opposite signs. The vector modes under such a perturbation ($\widetilde{EH}_{6,1}^{\text{even}}$) remain a linear combination of perturbed OAM modes, but they are now projected onto two degenerate vector modes $EH_{6,1}^{\text{even}}$ and $EH_{6,1}^{\text{odd}}$, as shown in Eq. (9). Hence, out-of-plane geometric perturbations fundamentally lead to mode mixing in the vector basis but not in the OAM basis. Note that this result follows previous experiments on geometric phases [78, 79], but here, realistic lengths of fibers could be used, by contrast, because the ring-core fiber design and use of high $|L|$ modes helped avoid the competing effects of mode coupling due to bends and birefringence. Although the length of fiber used in this experiment was only 4 m, OAM stability in ring core fibers has been observed up to 13.4 km propagation lengths [84].

$$\begin{cases} \widetilde{OAM}_{+L}^- = OAM_{+L}^- e^{i\phi_g} \\ \widetilde{OAM}_{-L}^+ = OAM_{-L}^+ e^{-i\phi_g} \end{cases} \quad (8)$$

$$\begin{cases} \widetilde{EH}_{L-1,1}^{\text{even}} = \frac{1}{2} \left(\widetilde{OAM}_{+L}^- + \widetilde{OAM}_{-L}^+ \right) = \cos \phi_g \cdot EH_{L-1,1}^{\text{even}} - \sin \phi_g \cdot EH_{L-1,1}^{\text{odd}} \\ \widetilde{EH}_{L-1,1}^{\text{odd}} = \frac{1}{2i} \left(\widetilde{OAM}_{+L}^- - \widetilde{OAM}_{-L}^+ \right) = \sin \phi_g \cdot EH_{L-1,1}^{\text{even}} + \cos \phi_g \cdot EH_{L-1,1}^{\text{odd}} \end{cases} \quad (9)$$

4 Geometric phase control

To quantitatively study the effect of geometric phase on high $|L|$ modes, we configure the fiber into a uniform helix shown in Figure 6(a). Input and output OAM and vector modes are shown schematically, for visual clarity. Although both feature a donut-shaped intensity profile, the illustrations here show spiral patterns for OAM modes, obtained when an OAM mode is interfered with an expanded Gaussian (with the number and orientation of parastiches denoting L and its sign, respectively). Likewise vector modes are schematically illustrated by their projection patterns, obtained when they are imaged through a polarizer (with the number of “beads” denoting $|2L|$). Figure 6(b) shows that the k -vector of light in a helical path encloses a solid angle, Ω . As the fiber helix is compressed, the solid angle increases accordingly, resulting in an extra geometric phase of the beam traveling in the fiber, without changing the path length of the light (and hence its dynamic phase). This solid angle is related to the period of the helix Λ , by $\Omega = 2\pi(1 - \Lambda/l)$, where l represents the length of fiber in one loop [75]. This helical arrangement is realized by loosely inserting the fiber into a Teflon tube with 1-mm inner diameter to minimize any torsion, stress,

or stretching during winding. This Teflon tube is then adhered to a metal spring, with which solid angle Ω can be controllably varied. This level of care is not needed for the OAM mode, which is stable, but is required for the vector mode, which, as shown in Figure 5(g) is sensitive to 3D fiber movement. Part of a 3.4-m-long segment of a ring-core fiber of length is wound into a uniform helix of 6.5 loops (light propagating in and out of fibers are in opposite directions). The length of each loop l is 16.3 cm. Note that the k -vector of the mode in the fiber, with magnitude β (its propagation constant), is well approximated to be parallel to the axis of the fiber under the weakly guiding approximation. Therefore, the solid angle subtended by the k -vector is approximately equal to the solid angle spanned by the fiber’s path, which follows that of the metal spring. As the spring is compressed, the pitch period Λ decreases from 2.3 to 0.2 cm, and the solid angle correspondingly increases from 1.72π to 1.96π . The total geometric phase acquired for a mode in this setup is equal to the geometric phase acquired in one loop multiplied by the number of loops N , as shown in Eq. (10):

$$\phi_g(C) = -N(\sigma + L)\Omega(C) \quad (10)$$

For an OAM mode with $L = -7\sigma^+$, the extra geometric phase results in a counterclockwise rotation of the beam. This rotation angle is equal to the additional phase divided by OAM order L , or $\Theta = \phi_g(C)/L$. Similarly, an OAM mode with $L = +7\sigma^-$ would obtain an extra geometric phase of the same amount but with opposite sign. As the signs of both OAM order and geometric phase are flipped, the beam rotation would have the same magnitude and direction. Therefore, the vector modes ($EH_{6,1}$ odd/even), which are the combinations of the two degenerate OAM modes, rotate counterclockwise with the same angle (shown schematically on the output patterns of Figure 6(a)). However, this rotation would lead to power oscillation between the odd and even degenerate vector modes because they are not rotationally invariant.

Figure 6(c) shows the measured power fluctuations between even and odd modes as the spring is gradually compressed, for an input comprising a pure $EH_{6,1}^{\text{even}}$ mode. As with the previous experiment of Figure 5(g), the two degenerate vector modes mix completely. The main difference is that the oscillation is now periodic and systematic because the geometric phase is accumulated monotonically, in a controlled fashion, with the helical arrangement. Based on the rotation angle of the vector modes, the accumulated geometric phase of the OAM modes can be calculated. As shown in Figure 6(d), the geometric phase shows a linear relationship with the solid

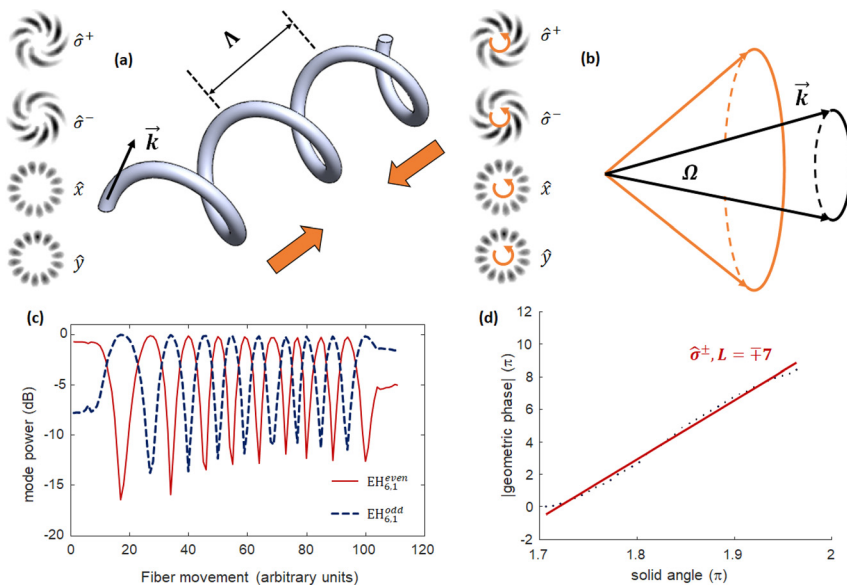


Figure 6: Systematic control of Pancharatnam–Berry phases in optical fibers.

(a) An orbital angular momentum (OAM) mode supporting ring-core fiber, inserted in a loose Teflon tube, is attached to a flexible spring to configure a helical with variable period Λ . A combination of two degenerate OAM modes ($L = -7\hat{\sigma}^+$ and $L = +7\hat{\sigma}^-$) is launched into the fiber. For visual clarity, the OAM modes are illustrated with spiral patterns that arise from their interference with an expanded Gaussian beam. The corresponding projection of this superposition state into \hat{x} and \hat{y} polarization-bins yields petal patterns, illustrated at the bottom left hand side of (a). The mode illustrations on the right side of the helical arrangement show the corresponding modes at the output of the fiber, all of which are rotated counterclockwise due to the geometrical transformation; (b) Geometric illustration of the solid angle Ω enclosed by the k -vector of the light path in this helical arrangement. The illustration in orange depicts the higher Ω obtained from compressing a spring from its original state, depicted in the black illustration; (c) Measured power fluctuations between even and odd modes for EH_{61} , using the reciprocal mode transmission setup of Figure 5(a), when the spring was compressed (pitch period Λ decreases from 2.3 to 0.2 cm). The uneven periodicity results from the uneven speed with which the spring was compressed; (d) Geometric phase, measured from vector mode power ratios, versus solid angle, for two degenerate OAM modes $L = -7\hat{\sigma}^+$ and $L = +7\hat{\sigma}^-$ as the helical spring is compressed. The red line is a linear fit of the experimental data (solid circles). Near-linear relationship shows exclusive influence of fiber path on geometric phase, and hence relative mode amplitudes.

angle, which matches the theoretical prediction (Eq. (10)) of a linear relationship between these parameters. It clearly shows that image rotation, and hence mixing, of vector modes is linearly proportional to the solid angle enclosed by the k -vector of light.

We repeat this experiment on five other pairs of modes that are stable in this ring-core fiber. As shown in Figure 7(a), the geometric phase shows a linear relationship with the solid angle in all cases. As evident, image rotation, and hence vector mode instability, increases as the TAM (equal to $L + \sigma$) of participating modes increases. Figure 7(b) shows that the slopes for each pair of OAM modes is linearly proportional to the TAM of the corresponding OAM modes. The magnitude of this slope (i.e., slope of the slopes vs. TAM), which is, effectively the number of loops N (per Eq. (10)), is 6.2, which is close to the expected value of $N = 6.5$. The lack of a better match may be due to the fact that input mode purity was only 10 dB, but even so, this confirms that the perturbations experienced

by these modes predominantly arise from the experimentally induced geometric, and not inadvertent bend or birefringence, perturbations

While the controlled experiments helped rigorously verify the influence of different kinds of perturbations on an optical fiber and, especially, their influence on different modes, the results of Figure 7(a) also point to applications toward a novel type of shape sensor, with sensitivity controlled by the OAM content of light in a fiber. One key distinction from other types of interferometric sensors that depend on the conventional dynamic phase of light is that this depends only on geometry. As mentioned earlier, dynamic phase arises from $e^{i\beta z}$, which is strongly wavelength dependent. By contrast, there is no wavelength dependence in geometric phase, meaning that its sensitivity does not depend on the bandwidth of the source, facilitating the use of low-cost sources even in high-sensitivity applications. Likewise, the lack of dynamic phase dependence also makes such sensors robust to ambient perturbations,

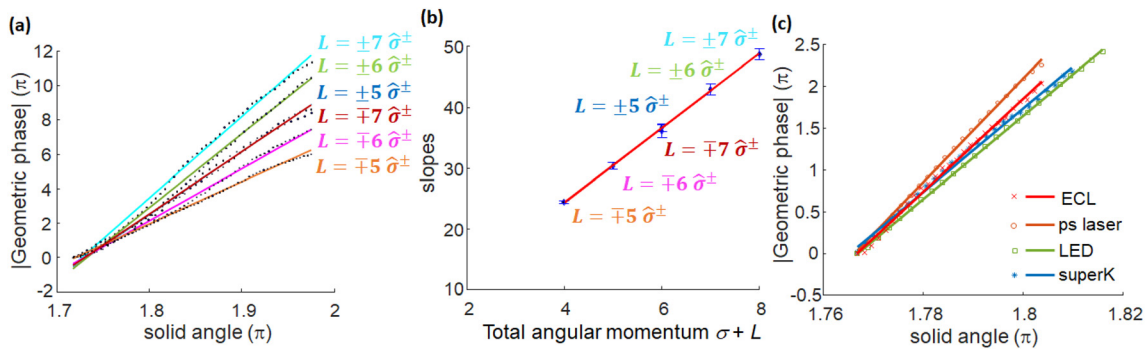


Figure 7: (a) Geometric phase versus fiber path solid angle for six distinct pairs of orbital angular momentum (OAM) modes. The colored lines are linear fits of the experimental data (black solid circles). All modes show a clear linear relationship; (b) The slope of each trace (for each mode) shown in (a) versus the TAM = $L + \sigma$ of the respective modes. The high degree of linearity as well as the slope of this line match well with theory that accounts only for geometric effects; (c) Geometric phase versus solid angle for two degenerate OAM modes $L = \pm 7\sigma^\pm$ (as shown earlier in (a)), using multiple light sources. External cavity laser (ECL) is a narrow linewidth (100 kHz) source at 1550 nm; ps laser is a picosecond laser at 1550 nm with ~ 0.5 nm bandwidth; the LED has a bandwidth ~ 35 nm around 1525 nm; superK represents a supercontinuum source with 3 dB bandwidth up to ~ 250 nm at around 1475 nm. Similar slopes for all these sources demonstrates weak dependence of wavelength on geometric phase.

such as temperature or pressure induced changes of the refractive index of the fiber.

To demonstrate this independence to wavelength, we conduct the same helix experiment with $|L| = 7$ SOa modes ($L = \pm 7\sigma^\pm$) using light sources of different bandwidths. Figure 7(c) shows the measured geometric phase as a function of solid angle, just as in Figures 6(d) and 7(a), when using sources of varying bandwidths. ECL denotes a narrow-linewidth (100 kHz) source at 1550 nm; “ps laser” is a picosecond laser at 1550 nm with ~ 0.5 nm bandwidth; the LED has a bandwidth ~ 35 nm around 1525 nm; and “superK” represents a supercontinuum source with 3-dB bandwidth of ~ 250 nm centered at ~ 1475 nm. The spatial interferometry method used to previously guarantee mode purity does not work with broadband sources (because it utilizes *dynamic* phase!). Hence, the purity of OAM modes is adjusted to be higher than 15 dB using the ECL, as before, and then the light source is carefully switch to other broadband sources without disturbing alignment, expecting minimal changes in mode purity. The geometric phase shows a linear dependence on solid angle regardless of the bandwidth of light source, as shown in Figure 7(c). However, the slopes obtained with the broadband sources differ from that obtained with the ECL by up to 12%. The mismatch probably arises from the lack of our ability to maintain high-purity excitation with the broadband sources, a problem easily solved in the future with the plethora of emerging mode-conversion technologies for OAM fiber modes [85]. Nevertheless, the results point to a novel means of developing low-cost shape sensors that

are insensitive to environmental perturbations such as temperature, pressure, mechanical vibrations and bends, while maintaining high sensitivity.

5 Discussion, summary, and conclusions

In summary, the ability to excite and propagate specific individual or a subset of HOMs in an optical fiber enables a variety of applications ranging from scaling information capacity and enabling new nonlinear interactions, to new forms of sensors and photonic devices. The key in several of these applications is the ability to exploit specific, distinct characteristics of HOMs, such as enabling unique nonlinear coupling pathways, yielding large A_{eff} or tailor-able dispersion, and realizing large unmixed states of information carriers. In these applications, finding the subset of modes that propagate with high linear stability is of paramount importance. This linear stability is intimately connected to properties of the modes themselves (their angular momentum content, and even the mathematical basis used to describe them) as well as the form of perturbations a fiber encounters. Considering the two most common fiber perturbations – bends, which induce birefringence as well as OAM transfer, and light’s path memory, manifested in the 3D trace that light follows – we arrive at the following conclusions related to modal stability for HOMs (illustrated in Figure 8). The commonly used LP modes are actually linear combinations of eigenmodes of dissimilar phase velocities, and thus they are not

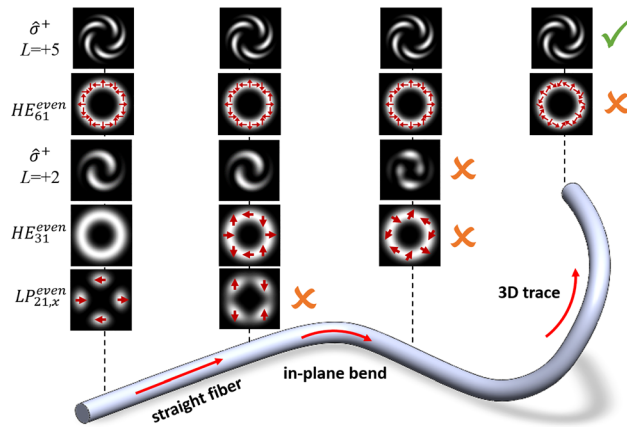


Figure 8: Summary of the propagation stability of optical fiber modes of different classes when the fiber is deployed with commonly encountered perturbations. The illustration depicts modes launched at the left end of a perfectly circular fiber, and all modes are schematically illustrated at four positions (black dashed lines) along the fiber propagation axis. From left to right: The input comprises pure modes in all the classes; the second position represents propagation through a straight fiber without any perturbations; this is followed by a position after propagation through a fiber that is bent only in plane; and, the final position represents propagation through a fiber that experiences an out-of-plane (3D) redirection as well. The modes from bottom to top represent LP modes ($LP_{2,1}$), low order vector modes ($EH_{3,1}^{even}$), low-order OAM modes ($L = 2\hat{\sigma}^+$), high-order vector modes ($EH_{6,1}^{even}$), and high-order OAM modes ($L = 5\hat{\sigma}^+$). After propagating through the straight fiber section, LP modes mix between orthogonal modes of the same class, whereas all the other modes remain stable. As such, LP modes, designated at this point with an orange cross, are not illustrated across subsequent perturbations, having failed to propagate through the most elementary arrangement. In-plane fiber bends easily couple a low-order vector ($EH_{3,1}^{even}$) or orbital angular momentum (OAM) ($L = 2\hat{\sigma}^+$) mode with its degenerate counterpart, while it does not impart enough angular momentum to couple a higher-order OAM mode $L = 5\hat{\sigma}^+$ or the corresponding vector mode $EH_{6,1}^{even}$ to their respective degenerate counterparts. Again, therefore, no further depiction of low L vector or OAM modes is illustrated (as indicated by the orange cross). After propagating through the 3D trace, a higher-order vector mode $EH_{6,1}^{even}$ mixes completely with its degenerate counterpart, whereas the corresponding OAM mode $L = 5\hat{\sigma}^+$ merely acquire a common geometric phase and remains remarkably stable. Hence, across all perturbations, only the high $|L|$ OAM mode survives without coupling, to its degenerate or nondegenerate counterparts.

translationally invariant even in a perfect, straight fiber. On the other hand, the vector and OAM modes, as two mathematically equivalent bases for mode representations, remain stable in an unperturbed fiber. However, when their modal index $|L|$ is low, they mix completely with their degenerate counterpart in a fiber that is bent (in-plane) because of birefringent coupling that couples polarizations

in SMFs too. High- $|L|$ vector and OAM modes are, by contrast, stable even across (in-plane) bent fibers because of inherent OAM conservation rules. Finally, when a fiber is not only bent, but also lifted out of plane, even high- $|L|$ vector modes become unstable, in that their polarization distributions rotate, because of the Pancharatnam–Berry phase that light accumulates in 3D paths. By contrast, a high- $|L|$ OAM mode remains remarkably stable, except for accumulating a common phase. Hence, as mode propagation is studied across a range of perturbations, starting from none (straight fiber) to bends, to, finally, 3D paths, modes of the same L and m indices, but represented in different mathematical bases are not, somewhat counter-intuitively, identical. Considering all these perturbations, OAM modes of sufficiently high $|L|$ are the most stable eigenmodes of a circularly symmetric optical fiber. A few important clarifications are in order: this stability is observable only once a fiber is designed such that n_{eff} splittings between pertinent nondegenerate modes is maximized, and this analysis ignores very long ($> \text{km}$) length propagation, where higher order effects of bends and twists may play a role. In such cases, one would expect modes of any class to mix, although the fundamental nature of the effects described here suggest that even in conditions where all modes mix, the circularly polarized OAM modes will likely be more robust compared with others. In addition, the OAM eigenbasis yields a stable platform in which to exploit path-memory effects arising from geometric transformations (Pancharatnam–Berry phases), which while studied extensively in free space, may now lead to new opportunities for wavelength-agnostic or wavelength-insensitive phase control with fibers. We expect that these findings will help inform the optimal modal basis to use in the variety of applications that envisage using HOMs of optical fibers.

Acknowledgments: The authors would like to thank Dr. P. Kristensen for manufacturing the ring-core fibers used in these experiments, and Drs. P.G. Kwiat, P. Gregg and G. Prabhakar for insightful discussions.

Author contribution: All the authors have accepted responsibility for the entire content of this submitted manuscript and approved submission.

Research funding: This work is supported, in part, by the Vannevar Bush Faculty Fellowship (N00014-19-1-2632), Brookhaven National Labs (Contract: 354281), Office of Naval Research MURI program (N00014-20-1-2450) and the National Science Foundation (ECCS-1610190).

Conflict of interest statement: The authors declare no conflicts of interest regarding this article.

References

- [1] H. H. Hopkins and N. S. Kapany, "A flexible fibre scope, using static scanning," *Nature*, vol. 173, pp. 39–41, 1954.
- [2] T. A. Birks, J. C. Knight, and P. J. St. Russell, "Endlessly single-mode photonic crystal fiber," *Opt. Lett.*, vol. 22, p. 961, 1997.
- [3] R. F. Cregan, B. J. Mangan, J. C. Knight, et al., "Singlemode photonic band gap guidance of light in air," *Science*, vol. 285, pp. 1537–1539, 1999.
- [4] F. Benabid, J. C. Knight, G. Antonopoulos, and P. J. St. Russell, "Stimulated Raman scattering in hydrogen-filled hollow-core photonic crystal fiber," *Science*, vol. 298, pp. 399–402, 2002.
- [5] P. Koplow, L. Goldberg, R. Moeller, and D. Klinder, "Singlemode operation of a coiled multimode fibre amplifier," *Opt. Lett.*, vol. 25, p. 442, 2000.
- [6] W. Wong, X. Peng, J. McLaughlin, and L. Dong, "Breaking the limit of maximum effective area for robust single-mode propagation in optical fibers," *Opt. Lett.*, vol. 30, pp. 2855–2857, 2005.
- [7] J. M. Fini, J. W. Nicholson, B. Mangan, et al., "Polarization maintaining single-mode low-loss hollow-core fibres," *Nat. Commun.*, vol. 5, p. 5085, 2014.
- [8] R. Ulrich, R. C. Rashleigh, and W. Eickhoff, "Bending-induced birefringence in single-mode fibers," *Opt. Lett.*, vol. 5, pp. 273–275, 1980.
- [9] P. K. A. Wai and C. R. Menyuk, "Polarization mode dispersion, decorrelation, and diffusion in optical fibers with randomly varying birefringence," *J. Lightwave Technol.*, vol. 14, pp. 148–157, 1996.
- [10] M. Brodsky, K. E. George, C. Antonelli, and M. Shtaif, "Loss of polarization entanglement in a fiber-optic system with polarization mode dispersion in one optical path," *Opt. Lett.*, vol. 36, pp. 43–45, 2011.
- [11] H. R. Stuart, "Dispersive multiplexing in multimode optical fiber," *Science*, vol. 289, pp. 281–283, 2000.
- [12] R. Ryf, N. K. Fontaine, S. Wittek, et al., "High-spectral-efficiency mode-multiplexed transmission over graded-index multimode fiber," in *ECOC'18*, 2018, Th3B.1.
- [13] B. Redding, S. M. Popoff, and H. Cao, "All-fiber spectrometer based on speckle pattern reconstruction," *Opt. Express*, vol. 21, pp. 6584–6600, 2013.
- [14] T. Cižmár and K. Dholakia, "Exploiting multimode waveguides for pure fibre-based imaging," *Nat. Commun.*, vol. 3, p. 1027, 2012.
- [15] N. Borhani, E. Kakkava, C. Moser, and D. Psaltis, "Learning to see through multimode fibers," *Optica*, vol. 5, pp. 960–966, 2018.
- [16] A. Hasegawa, "Self-confinement of multimode optical pulse in a glass fiber," *Opt. Lett.*, vol. 5, pp. 416–417, 1980.
- [17] L. G. Wright, D. N. Christodoulides, and F. W. Wise, "Controllable spatiotemporal nonlinear effects in multimode fibres," *Nat. Photonics*, vol. 9, pp. 306–310, 2015.
- [18] K. Krupa, A. Tonello, B. M. Shalaby, et al., "Spatial beam self-cleaning in multimode fibres," *Nat. Photonics*, vol. 11, pp. 237–241, 2017.
- [19] K. Krupa, A. Tonello, A. Barthélémy, et al., "Observation of geometric parametric instability induced by the periodic spatial self-imaging of multimode waves," *Phys. Rev. Lett.*, vol. 116, p. 183901, 2016.
- [20] A. W. Snyder and J. D. Love, *Optical Waveguide Theory*, London, U.K., Chapman and Hall, 1983.
- [21] A. Ghatak and W. J. Thyagarajan, *Introduction to Fiber Optics*, Cambridge, U.K., Cambridge University Press, 1998.
- [22] C. D. Poole, J. M. Weisenfeld, D. J. DiGiovanni, and A. M. Vengsarkar, "Optical fiber-based dispersion compensation using higher order modes near cutoff," *J. Lightwave Technol.*, vol. 12, pp. 1746–1758, 1994.
- [23] S. Ramachandran, S. Ghalmi, J. W. Nicholson, et al., "Anomalous dispersion in a solid, silica-based fiber," *Opt. Lett.*, vol. 31, pp. 2532–2534, 2006.
- [24] S. Ramachandran, B. Mikkelsen, L. C. Cowsar, et al., "All-fiber grating-based higher order mode dispersion compensator for broad-band compensation and 1000-km transmission at 40 Gb/s," *IEEE Photonics Technol. Lett.*, vol. 13, pp. 632–634, 2001.
- [25] A. H. Gnauck, L. D. Garrett, Y. Danziger, U. Levy, and M. Tur, "Dispersion and dispersion-slope compensation of NZDSF over the entire C band using higher-order-mode fibre," *Electron. Lett.*, vol. 36, pp. 1946–1947, 2000.
- [26] S. Ramachandran, M. F. Yan, J. Jasapara, et al., "High-energy (nanojoule) femtosecond pulse delivery with record dispersion higher-order mode fiber," *Opt. Lett.*, vol. 30, pp. 3225–3227, 2005.
- [27] R. H. Stolen, J. E. Bjorkholm, and A. Ashkin, "Phase-matched three-wave mixing in silica fiber optical waveguides," *Appl. Phys. Lett.*, vol. 24, no. 7, pp. 308–310, 1974.
- [28] J. Demas, P. Steinurzel, B. Tai, L. Rishøj, Y. Chen, and S. Ramachandran, "Intermodal nonlinear mixing with Bessel beams in optical fiber," *Optica*, vol. 2, pp. 14–17, 2015.
- [29] J. Demas, L. Rishøj, X. Liu, G. Prabhakar, and S. Ramachandran, "Intermodal group-velocity engineering for broadband nonlinear optics," *Photonics Res.*, vol. 7, pp. 1–7, 2019.
- [30] L. Rishøj, B. Tai, P. Kristensen, and S. Ramachandran, "Soliton self-mode conversion: revisiting Raman scattering of ultrashort pulses," *Optica*, vol. 6, pp. 304–308, 2019.
- [31] P. J. St. Russell, R. Culverhouse, and F. Farahi, "Experimental observation of forward stimulated Brillouin scattering in dual-mode single core fiber," *Electron. Lett.*, vol. 26, pp. 1195–1196, 1990.
- [32] F. G. Omenetto, A. J. Taylor, M. D. Moores, et al., "Simultaneous generation of spectrally distinct third harmonics in a photonic crystal fiber," *Opt. Lett.*, vol. 26, pp. 1158–1160, 2001.
- [33] A. Efimov, A. J. Taylor, F. G. Omenetto, J. C. Knight, W. J. Wadsworth, and P. J. St. Russell, "Nonlinear generation of very high-order UV modes in microstructured fibers," *Opt. Express*, vol. 11, pp. 910–918, 2003.
- [34] J. Demas, G. Prabhakar, T. He, and S. Ramachandran, "Wavelength-agile high-power sources via four-wave mixing in higher-order fiber modes," *Opt. Express*, vol. 25, pp. 7455–7464, 2017.
- [35] D. Cruz-Delgado, R. Ramirez-Alarcon, E. Ortiz-Ricardo, et al., "Fiber-based photon-pair source capable of hybrid entanglement in frequency and transverse mode, controllably scalable to higher dimensions," *Sci. Rep.*, vol. 6, p. 27377, 2016.
- [36] S. Ramachandran, J. W. Nicholson, S. Ghalmi, et al., "Light propagation with ultra-large modal areas in optical fibers," *Opt. Lett.*, vol. 31, pp. 1797–9, 2006.
- [37] K. S. Abedin, R. Ahmad, A. M. De Santolo, and D. J. DiGiovanni, "Reconversion of higher-order-mode (HOM) output from cladding-pumped hybrid Yb:HOM fiber amplifier," *Opt. Express*, vol. 27, pp. 8585–8595, 2019.
- [38] K. Rottwitt, J. G. Koefoed, K. Ingerslev, and P. Kristensen, "Intermodal Raman amplification of OAM fiber modes," *APL Photonics*, vol. 4, p. 030802, 2019.
- [39] X. Liu, E. N. Christensen, K. Rottwitt, and S. Ramachandran, "Nonlinear four-wave mixing with enhanced diversity and

selectivity via spin and orbital angular momentum conservation," *APL Photonics*, vol. 5, p. 010802, 2020.

[40] S. Zhu, S. Pachava, S. Pidishety, Y. Feng, B. Srinivasan, and J. Nilsson, "Raman amplification of charge-15 orbital angular momentum mode in a large core step index fiber," in *CLEO*, 2020, SM1P.2.

[41] L. Yan, P. Kristensen, and S. Ramachandran, "Vortex fibers for STED microscopy," *APL Photonics*, vol. 4, p. 022903, 2019.

[42] B. M. Heffernan, S. A. Meyer, D. Restrepo, M. E. Siemens, E. A. Gibson, and J. T. Gopinath, "A fiber-coupled stimulated emission depletion microscope for bend-insensitive through-fiber imaging," *Sci. Rep.*, vol. 9, p. 11137, 2019.

[43] M. Fridman, G. Machavariani, N. Davidson, and A. A. Friesem, "Fiber lasers generating radially and azimuthally polarized light," *Appl. Phys. Lett.*, vol. 93, p. 191104, 2008.

[44] N. Bozinovic, Y. Yue, Y. Ren, et al., "Terabit-scale orbital angular momentum mode division multiplexing in fibers," *Science*, vol. 340, pp. 1545–1548, 2013.

[45] J. Liu, L. Zhu, A. Wang, et al., "All-fiber pre- and post-data exchange in km-scale fiber-based twisted lights multiplexing," *Opt. Lett.*, vol. 41, pp. 3896–3899, 2016.

[46] R. M. Nejad, K. Allahverdyan, P. Vaity, et al., "Mode division multiplexing using orbital angular momentum modes over 1.4 km ring core fiber," *J. Lightwave Technol.*, vol. 34, pp. 4252–4258, 2016.

[47] G. Zhu, Z. Hu, X. Wu, et al., "Scalable mode division multiplexed transmission over a 10-km ring-core fiber using high-order orbital angular momentum modes," *Opt. Express*, vol. 26, pp. 594–604, 2018.

[48] K. Ingerslev, P. Gregg, M. Galili, et al., "12 mode, WDM, MIMO-free orbital angular momentum transmission," *Opt. Express*, vol. 26, pp. 20225–20232, 2018.

[49] D. Cozzolino, D. Bacco, B. Da Lio, et al., "Orbital angular momentum states enabling fiber-based high-dimensional quantum communication," *Phys. Rev. Appl.*, vol. 11, p. 064058, 2019.

[50] S. Ramachandran, Z. Wang, and M. F. Yan, "Bandwidth control of long-period grating-based mode-converters in few-mode fibers," *Opt. Lett.*, vol. 27, pp. 698–700, 2002.

[51] M. Tur, D. Menashe, Y. Japha, and Y. Danziger, "High-order mode based dispersion compensating modules using spatial mode conversion," *J. Opt. Fiber Commun. Rep.*, vol. 5, pp. 249–311, 2007.

[52] L. Marrucci, E. Karimi, S. Slussarenko, et al., "Spin-to-orbital conversion of the angular momentum of light and its classical and quantum applications," *J. Opt.*, vol. 13, p. 064001, 2011.

[53] A. Astorino, J. Glückstad, and K. Rottwitt, "Fiber mode excitation using phase-only spatial light modulation: guideline on free-space path design and lossless optimization," *AIP Adv.*, vol. 8, p. 095111, 2018.

[54] Y. Zhao, J. Zhang, J. Du, and J. Wang, "Meta-facet fiber for twisting ultra-broadband light with high phase purity," *Appl. Phys. Lett.*, vol. 113, p. 061103, 2018.

[55] R. Olszansky, "Mode coupling effects in graded-index optical fibers," *Appl. Opt.*, vol. 14, pp. 935–945, 1975.

[56] S. Savović and A. Djordjević, "Solution of mode coupling in step index optical fibers by Fokker–Planck equation and Langevin equation," *Appl. Opt.*, vol. 41, pp. 2826–2830, 2002.

[57] S. Ramachandran and P. Kristensen, "Optical vortices in fiber," *Nanophotonics Berlin*, vol. 2, pp. 455–74, 2013.

[58] A. M. Yao and M. J. Padgett, "Orbital angular momentum: origins, behaviour and applications," *Adv. Opt. Photonics*, vol. 3, pp. 161–204, 2011.

[59] A. Bjarklev, "Microdeformation losses of single-mode fibers with step-index profiles," *J. Lightwave Technol.*, vol. 4, pp. 341–346, 1986.

[60] S. Ramachandran and M. F. Yan, "Static and tunable dispersion management with higher order mode fibers," in *Fiber Based Dispersion Compensation*, S. Ramachandran, Ed., New York, Springer, 2007.

[61] M. Tur, D. Menashe, Y. Japha, and Y. Danziger, "High-order mode based dispersion compensating modules using spatial mode conversion," *J. Opt. Fiber Commun. Rep.*, vol. 5, pp. 249–311, 2007.

[62] S. Ramachandran, J. M. Fini, M. Mermelstein, J. W. Nicholson, S. Ghalmi, and M. F. Yan, "Ultra-large effective-area, higher-order mode fibers: a new strategy for high-power lasers. Invited Paper," *Laser Photonics Rev.*, vol. 2, pp. 429–48, 2008.

[63] J. W. Nicholson, J. M. Fini, A. M. DeSantolo, et al., "Scaling the effective area of higher-order-mode erbium-doped fiber amplifiers," *Opt. Express*, vol. 20, pp. 24575–24584, 2012.

[64] S. Ramachandran, S. Golowich, M. F. Yan, et al., "Lifting polarization degeneracy of modes by fiber design: a platform for polarization-insensitive microbend fiber gratings," *Opt. Lett.*, vol. 30, pp. 2864–2866, 2005.

[65] S. Ramachandran, P. Kristensen, and M. F. Yan, "Generation and propagation of radially polarized beams in optical fibers," *Opt. Lett.*, vol. 34, pp. 2525–2527, 2009.

[66] B. Ung, P. Vaity, L. Wang, Y. Messadeq, L. A. Rusch, and S. LaRochelle, "Few-mode fiber with inverse parabolic graded-index profile for transmission of OAM-carrying modes," *Opt. Express*, vol. 22, pp. 18044–18055, 2014.

[67] C. Brunet, B. Ung, P. A. Belanger, Y. Messadeq, S. LaRochelle, and L. A. Rusch, "Vector mode analysis of ring-core fibers: design tools for spatial division multiplexing," *J. Lightwave Technol.*, vol. 32, pp. 4046–4057, 2014.

[68] S. Ramachandran, P. Gregg, P. Kristensen, and S. E. Golowich, "On the scalability of ring fiber designs for OAM multiplexing," *Opt. Express*, vol. 23, pp. 3721–3730, 2015.

[69] P. Gregg, P. Kristensen, A. Rubano, S. Golowich, L. Marrucci, and S. Ramachandran, "Enhanced spin orbit interaction of light in highly confining optical fibers for mode division multiplexing," *Nat. Commun.*, vol. 10, p. 4707, 2019.

[70] D. L. P. Vitullo, C. C. Leary, P. Gregg, et al., "Observation of interaction of spin and intrinsic orbital angular momentum of light," *Phys. Rev. Lett.*, vol. 118, p. 083601, 2017.

[71] N. Bozinovic, S. Golowich, P. Kristensen, and S. Ramachandran, "Control of orbital angular momentum of light with optical fibers," *Opt. Lett.*, vol. 37, p. 2451, 2012.

[72] P. Gregg, P. Kristensen, and S. Ramachandran, "Conservation of orbital angular momentum in air-core optical fibers," *Optica*, vol. 2, p. 267, 2015.

[73] S. Pancharatnam, "Generalized theory of interference and its applications. Part I. Coherent pencils," *Proc. Indiana Acad. Sci.*, vol. A44, p. 247, 1956.

[74] M. V. Berry, "Quantal phase factors accompanying adiabatic changes," *Proc. R. Soc. Lond. A.* vol. 392, pp. 45–57, 1984.

- [75] A. Tomita and R. Y. Chiao, "Observation of Berry's topological phase by use of an optical fiber," *Phys. Rev. Lett.*, vol. 57, pp. 937–940, 1986.
- [76] R. A. Beth, "Mechanical detection and measurement of the angular momentum of light," *Phys. Rev.*, vol. 50, pp. 115–25, 1936.
- [77] M. Berry, "Anticipations of the geometric phase," *Phys. Today*, vol. 43, pp. 34–40, 1990.
- [78] J. Anandan, "The geometric phase," *Nature*, vol. 360, pp. 307–313, 1992.
- [79] K. Y. Bliokh, "Geometrical optics of beams with vortices: berry phase and orbital angular momentum Hall effect," *Phys. Rev. Lett.*, vol. 97, p. 043901, 2006.
- [80] S. Abdulkareem and N. Kundikova, "Joint effect of polarization and the propagation path of a light beam on its intrinsic structure," *Opt. Express*, vol. 24, p. 19157, 2016.
- [81] X. Huang, S. Gao, B. Huang, and W. Liu, "Demonstration of spin and extrinsic orbital-angular-momentum interaction using a few-mode optical fiber," *Phys. Rev. A*, vol. 97, p. 033845, 2018.
- [82] Z. Ma, G. Prabhakar, P. Gregg, and S. Ramachandran, "Robustness of OAM fiber modes to geometric perturbations," in *Conference on Lasers and Electro-Optics*, 2018.
- [83] P. Gregg, M. Mirhosseini, A. Rubano, et al., "Q-plates as higher order polarization controllers for orbital angular momentum modes of fiber," *Opt. Lett.*, vol. 40, p. 1729, 2015.
- [84] P. Gregg, P. Kristensen, and S. Ramachandran, "13.4 km OAM state propagation by recirculating fiber loop," *Opt. Express*, vol. 24, pp. 18938–18947, 2016.
- [85] X. Wang, Z. Nie, Y. Liang, J. Wang, T. Li, and B. Jia, "Recent advances on optical vortex generation," *Nanophotonics*, vol. 7, pp. 1533–1556, 2018.